

Spatiotemporally Coherent Probabilistic Generation of Weather from Climate

Jonathan Schmidt, Luca Schmidt, Felix Strnad, Nicole Ludwig, Philipp Hennig
University of Tübingen, Tübingen AI Center
Tübingen, Germany

Abstract Local climate information is crucial for impact assessment and decision-making, yet coarse global climate simulations cannot capture small-scale phenomena. Current statistical downscaling methods infer these phenomena as temporally decoupled spatial patches. However, to preserve physical properties, estimating spatio-temporally coherent high-resolution weather dynamics for multiple variables across long time horizons is crucial. We present a novel generative approach that uses a score-based diffusion model trained on high-resolution reanalysis data to capture the statistical properties of local weather dynamics. After training, we condition on coarse climate model data to generate weather patterns consistent with the aggregate information. As this inference task is inherently uncertain, we leverage the probabilistic nature of diffusion models and sample multiple trajectories. We evaluate our approach with high-resolution reanalysis information before applying it to the climate model downscaling task. We then demonstrate that the model generates spatially and temporally coherent weather dynamics that align with global climate output.

Numerical simulations based on the Navier-Stokes equations, discretized over time and space, are fundamental to understanding weather patterns, climate variability, and climate change. State-of-the-art numerical weather prediction (NWP) models, which primarily focus on atmospheric processes, can accurately resolve small-scale dynamics within the Earth system, providing fine-scale spatial and temporal weather patterns at resolutions on the order of kilometers [1]. However, the substantial computational resources required for these models render them impractical for simulating the extended time scales associated with climatic changes. In contrast, Earth System Models (ESMs), such as those included in the CMIP6 project [2], incorporate a broader range of processes—including atmospheric, oceanic, and biogeochemical interactions—while operating on coarser spatial scales. Typical grid resolutions for ESMs are approximately 1° , equivalent to around 100 km. This coarse resolution limits the ability of ESMs to fully capture small-scale processes, requiring parameterizations to represent unresolved dynamics as functions of resolved variables.

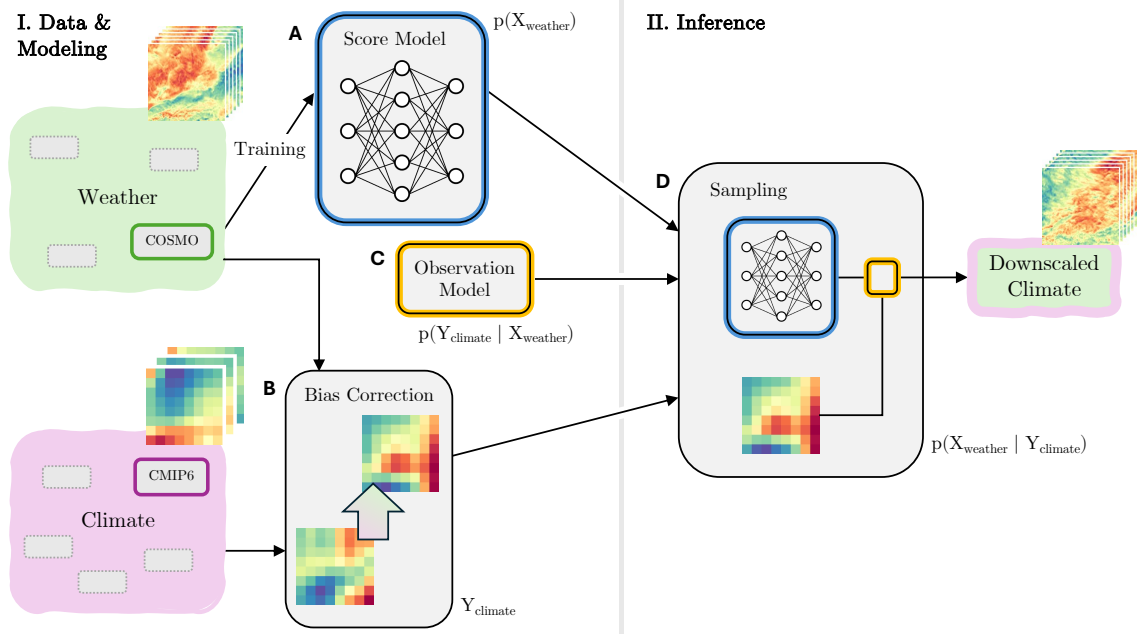


Figure 1: **Probabilistic pipeline for spatiotemporal downscaling of multiple variables.** This work introduces a probabilistic downscaling pipeline that jointly estimates spatio-temporally consistent weather dynamics from ESM simulations on multiple variables. The framework is built around a score-based diffusion model and can be understood as a combination of four modules, which can each be adjusted independently of the others. This schematic outlines the framework. Only one exemplary variable is shown for visual clarity. **A:** A diffusion model is trained on reanalysis data. For a pre-defined set of variables, it learns to reproduce the spatial and temporal patterns from the reanalysis data it is trained on. Note that ESM simulations are not part of the training process. **B:** From any ESM (e.g. CMIP6), select and pre-process an ensemble run (e.g. MPI-HR) for downscaling. A bias-correction step that partially mitigates distributional deviations between simulated climate and reanalysis data can be applied to the climate input as a pre-processing step. **C:** Formulate a known or assumed functional relationship between climate and weather dynamics. This step imposes a constraint onto the generative model such that its samples adhere to the encoded prior knowledge. **D:** The model generates weather trajectories that preserve the statistics of the coarse climate input. During the generative process, the trained score model (**A**) is conditioned to fulfill the constraint imposed by explicitly relating the conditioning information (**B**) to the generated samples through the observation model (**C**).

These parameterizations reduce the local detail in ESM outputs, introducing a scale mismatch between modeled outputs and the fine-scale processes that influence local climate. Consequently, ESM data cannot be directly employed to evaluate changes at the local scale, restricting their utility for localized decision-making. To address this limitation, novel approaches are needed to infer local dynamics from coarse-grained models while preserving their global-scale information. Machine learning (ML), particularly techniques derived from image generation, offers a promising avenue for overcoming these challenges. Statistical downscaling methods powered by ML enhance the spatial and temporal resolution of ESM outputs, providing detailed local information and addressing the limitations of traditional modeling approaches. Despite their promise, applying ML to climate modeling presents a significant challenge. ESMs are designed to generate accurate multi-decadal summary statistics, which inherently differ from historical observational datasets. This misalignment complicates the training of ML models, which typically require well-aligned datasets to optimize the model by minimizing the difference between simulations and observations. Generative models, a subset of ML techniques, offer a potential solution. Unlike other ML approaches, generative models learn the underlying data distribution, enabling them to generate plausible sample trajectories. Recent methodological advances in generative modeling [3–5], in particular a diffusion model designed to emulate physically plausible dynamics that are conditioned on known or assumed relationships between observed and predicted quantities [6], allows bridging the gap between coarse-resolution ESM outputs and fine-scale local processes, thereby enhancing the utility of ESMs for localized and regional analyses, even in the context of future climate projections.

We leverage and extend the score-based diffusion generative model of Rozet and Louppe [6] (Figure 1) to (simultaneously) increase the spatial and temporal resolution of multivariate coarse climate model output. We show that this approach enables high-fidelity realizations of local weather patterns. The model is first trained on high-resolution reanalysis data to capture the statistical and physical properties of local weather dynamics, after which it is conditioned on climate simulations for spatial and temporal downscaling. This framework requires an explicitly defined functional relationship between coarse-grained climate inputs and high-resolution weather outputs, thereby integrating prior knowledge into the modeling process. By separating the training of weather dynamics from task-specific inference, the model becomes highly flexible and versatile. This enables it to be applied to a range of tasks, including downscaling, which can be performed in a zero-shot manner without requiring retraining.

In our experiments, we demonstrate that this model generates weather sequences that are physically plausible, spatially and temporally consistent, and aligned with climate projections. The model effectively recovers local weather dynamics, including extreme events such as cyclones. Furthermore, its generative nature allows it to provide samples from the posterior distribution, enabling the generation of multiple plausible weather trajectories. This ability is crucial for assessing the variability and uncertainty, providing a comprehensive understanding of future weather scenarios.

Results

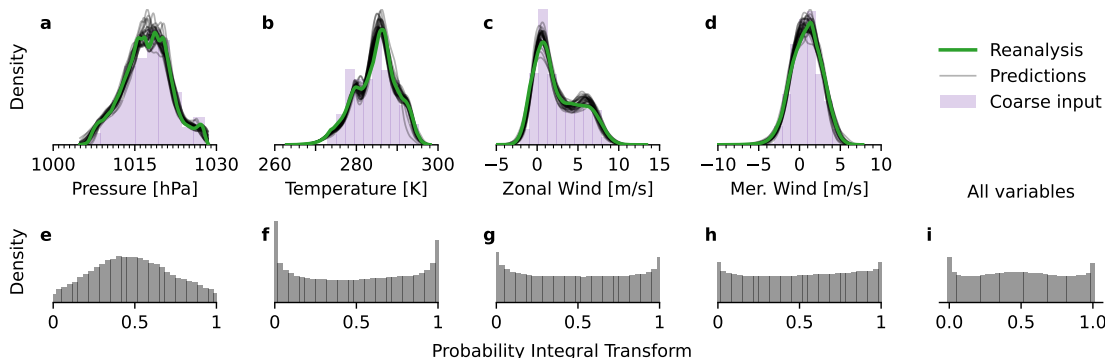


Figure 2: **Comparison of value distributions: reanalysis data, coarse input, predictions.** For a time range of 49 hours, this plot shows that the 1-hourly local predictions, which the model predicted from the coarse 6-hourly input, resemble the reanalysis data closely, in distribution. *Top row:* Kernel-density estimations for value distributions of reanalysis data (green) and 30 predictions (black). The prediction model was conditioned on coarse inputs (purple). The predicted samples align with the reanalysis data distribution, which is fully covered by the predictive uncertainty. *Bottom row:* The probability integral transform (PIT) assesses the uncertainty calibration of the model: for each variable separately (e–h) and overall (i). A PIT distribution that resembles a standard uniform distribution indicates that the reanalysis data and predictions likely come from the same distribution.

Evaluation of predictive distribution and uncertainty calibration

We first evaluate the methodological framework used for downscaling in an on-model setting. We construct an experimental setup with artificially coarsened reanalysis data that surrogates the ESM simulations. This setting simulates a direct pairing between the climate and reanalysis data. It thus allows for evaluating the model’s predictive capabilities and uncertainty quantification by comparing it to a ground truth. This setup is described in the Methods section.

From the coarse input data, the model predicts weather trajectories that match the reanalysis data in distribution when aggregated across space and time. Figure 2 a–d show that the estimated densities of the predictions cover those of the reanalysis data in the predicted uncertainty. In particular, the probabilistic model introduces no systematic biases, like distribution shift, a tendency towards over- or under-predicting values, or mismatch in the tail regions. Instead, each sampled prediction captures the spread of the data distribution. To assess the calibration of the predictive uncertainty, we compute the probability integral transform (PIT) for all values aggregated and for each variable separately. We find that both wind-speed components (Figure 2 g,h) are well calibrated. The predictions for mean sea-level pressure (Figure 2 e) are slightly too defensive, over-predicting extreme values. For surface temperature (Figure 2 f), the opposite is the case: the predicted distribution is slightly too narrow and under-predicts tail events. Overall (Figure 2 i), the model is well calibrated.

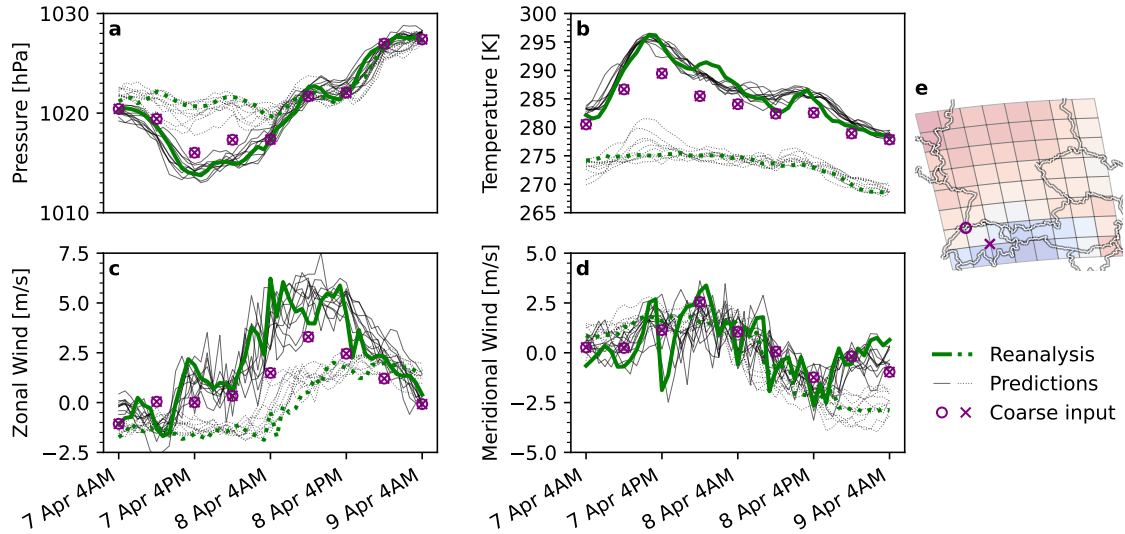


Figure 3: **Differences in local dynamics are inferred from coarse-grained observations.** This plot compares time series at two locations over 49 hours between reanalysis data (green), 30 predictions (black), and coarse input (purple) and shows that the model can accurately extract local dynamics from shared coarse information. Both fine-grid locations were selected to share a single point on the coarse grid (e). Each plot (a–d) shows one variable. Reanalysis and predicted weather trajectories are shown in solid and dotted lines for both locations, respectively. The conditioning information (purple circles and crosses) is a single value every six hours that is shared by both locations (e), at which the local weather dynamics are inferred. The predicted time series aligns with the reanalysis data at both locations. In particular, the uncertainty obtained through sampling multiple predictions covers the reanalysis data, and the individual samples mirror the local weather trajectories in their respective temporal structure.

Recovering local dynamics from coarse information

Recovering complex local dynamics from coarse information is a crucial requirement we impose on the downscaled predictions. This experiment shows that our model accurately predicts spatial and temporal variations in weather trajectories at two distinct locations, which share a single spatial observation. To this end, we investigate two locations with distinct weather dynamics that both lie in a region that corresponds to one node on the coarse observation grid (Figure 3 e). To ensure the model can recover meaningful local information from coarse information, we compare the temporal evolution of the downscaled trajectories at both locations in Figure 3. We find that the predictions’ time series align with the reanalysis data throughout the considered temporal period and across all variables. As an illustrative example, the zonal wind speeds (Figure 3 c), show substantial variability between the two locations—both in their values and their temporal structure. The model captures these variations in its predictions, highlighting its ability to recover local-scale variability lost in the coarse-resolution observations.

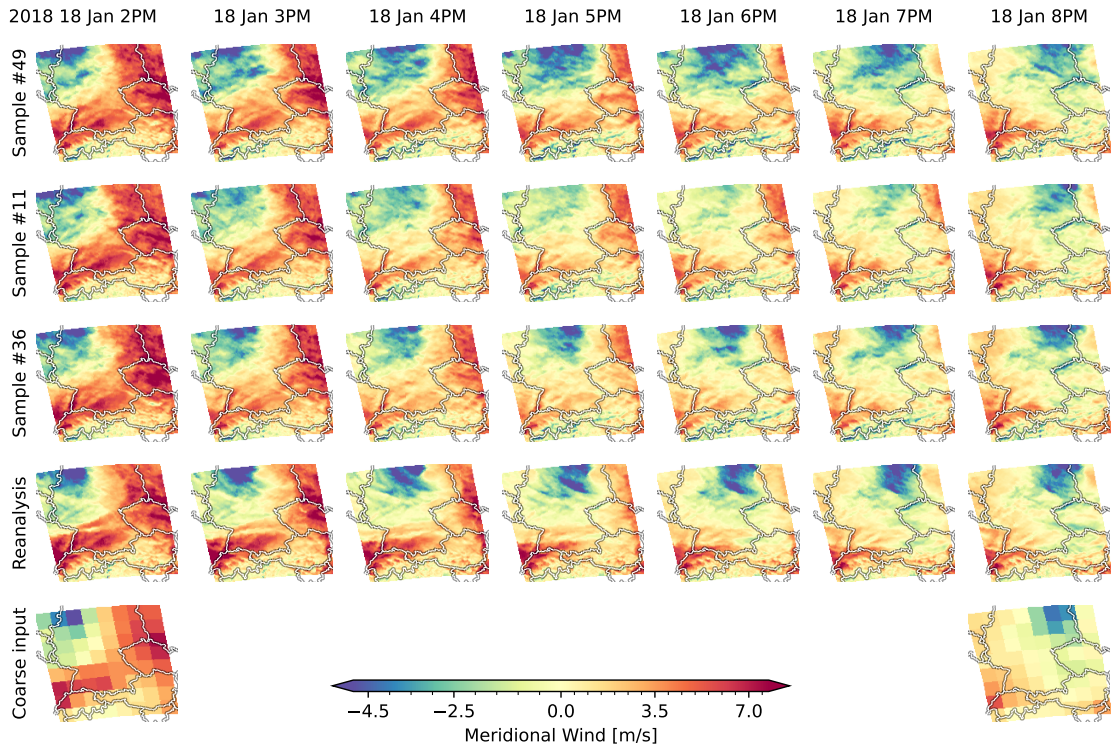


Figure 4: **Predicting high-resolution dynamics during a cyclone as an extreme event.** This plot shows meridional wind trajectories of three randomly selected model predictions (top three rows), reanalysis data (fourth row), and coarse conditioning information (bottom row) during a cyclone ("Friederike", January 2018). The sign of the wind speed value defines its direction: negative values go southward, and positive values go northward. Time progresses from left to right hourly, starting 2018 January 18 at 02:00 PM and ending the same day at 08:00 PM. Between the first (2:00 PM) and the last (8:00 PM) visualized time point, no information is provided to the model. The top three rows show how different samples fill in the missing spatial and temporal information. Each individual generated trajectory aligns visually with the coarse input, while the variation among the samples captures the uncertainty associated with the inference problem. Notably, the model does not introduce implausible "jumps" from one observation to the next but interpolates with spatially and temporally consistent dynamics.

Spatiotemporally consistent weather trajectories

Statistical downscaling is particularly challenging during extreme events since they are rare and thus lie in the tails of the training distribution while potentially involving highly complex dynamics. However, extreme events are particularly interesting, as they often have the most significant societal and environmental impacts. To assess the model performance in reproducing extreme events, we choose the time range in which cyclone "Friederike" approached central Europe (including the modeled spatial region) from the west around January 18, 2018. Aside from the time period, the

experimental setup remains unaltered from the above sections. This setting is especially challenging during a storm event since local spatial and temporal dynamics are hidden from the model and have to be inferred based on very scarce information. However, the sub-sampled observations are enough to guide the model in accurately predicting the cyclone. [Figure 4](#) shows the meridional wind trajectories during the event for three randomly selected model predictions, the reanalysis data, and the coarse conditioning information. While the samples have significant variation, all three predictions are consistent in space and time and plausibly explain the provided coarse observations. Furthermore, the radially-averaged power spectral density of the predictions closely matches the reanalysis data (supplementary [Figure A.2a](#)), showing the physical plausibility of the predictions.

Local climate information through downscaling

Through a series of experiments, we demonstrated that the model can infer small-scale dynamics from artificially coarsened data such that the predictions are spatially, temporally and physically plausible while preserving the underlying value distribution. Building on these findings, we now move to downscaling climate outputs, using 6-hourly CMIP6 ESM simulations as conditioning information. As in the previous experiments, the four variables considered are downscaled spatially (by a factor of 16×16) and temporally (by a factor of 6) to align with the resolution of the reanalysis data.

While this setup is similar to the previous experiments, differing only in the type of conditioning data, the problem is more challenging. Climate simulations and reanalysis data are not aligned; hence, we do not have access to ground truth (paired high- and low-resolution) data. Furthermore, raw climate model outputs typically contain systematic biases when compared to observational data. And ESM models are, of course, themselves subject to simulation error. As illustrated in the top row in [Figure 5](#), these biases result in systematic deviations between ESM outputs and reanalysis data distributions. We mitigate climate model biases using a per-variable quantile-mapping approach [7]. [Figure 5 \(a-d \$\mapsto\$ e-h\)](#) shows that the bias-correction step reduces the distributional shift between the climate and weather distribution.

Reducing the discrepancies between climate and weather distributions is not the task of the generative downscaling model but is instead addressed by a bias correction applied to the conditioning input. However, bias correction cannot resolve fundamental simulation errors in climate models [8]. Climate models are inherently imperfect representations of the climate system, with inaccuracies in parameterizations, simplified process representations, and uncertainties regarding the system’s initial state [9]. These variations lead to significant discrepancies between models; choosing a model, therefore, becomes a critical factor [10]. Even in the hypothetical case of perfect models (i.e., no epistemic uncertainty), forecasts are not deterministic due to the chaotic nature of the atmosphere. The internal variability of the climate system leads to differences between projected and observed climate [11]. This implies that climate simulations represent only one possible realization of the system with substantial uncertainty remaining. To illustrate this, [Figure 5](#) shows two model ensembles from different climate models: the MPI-HR and the HadGEM model. This illustrates that, even in terms of their aggregated-value distribution, climate model outputs can differ substantially from other ensembles and the reanalysis data.

[Figure 6](#) presents a qualitative assessment of the spatial and temporal progression of downscaled ESM simulations. The model output reproduces spatial patterns, such as the Alps, and temporal patterns, like the day-night cycle, while introducing local weather dynamics consistent with observations and propagating in a physically plausible manner. Together, [Figure 5](#) and [Figure 6](#) show that the

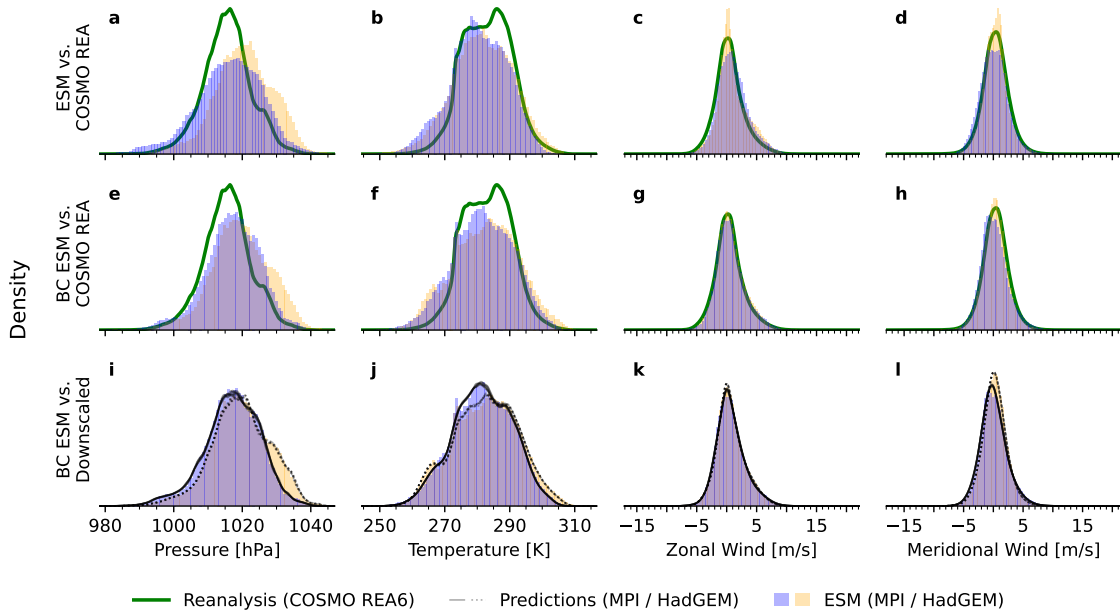


Figure 5: **Comparison of value distributions: ESM, de-biased ESM, reanalysis data, predictions.** This plot shows two things: firstly, the bias-correction reduces the distributional shift between ESM output and reanalysis data. Secondly, the model can generate high-resolution weather trajectories that introduce complex local weather dynamics while preserving the value distribution of the ESM simulations. Comparing the *top row* and the *middle row* shows that the distribution mismatch between both ESM ensembles and the reanalysis data (**a-d**) is mitigated through the bias-correction step (**e-h**). The *bottom row* shows that the distribution of the downscaled climate trajectories aligns with the coarse model input. The value histograms for the de-biased ESM data in the *bottom row* are copied over from the *middle row*. The considered time range is the year 2014; precisely 1-hourly steps starting January 01 at 06:00 AM and ending December 31 at 06:00 AM. Two distinct CMIP6 ensembles (MPI and HadGEM) are visualized together, which allows a comparison of the distributional mismatch between a) the respective climate simulations and b) the climate projections and the reanalysis data. For each ESM, eight downscaled samples are shown. The model does not introduce systematic biases, the downscaled ESM distributions are not shifted or skewed unexpectedly, and the tails align with their coarse counterparts.

model can generate high-resolution weather trajectories that introduce complex local dynamics while preserving the value distribution of the respective ESM simulations. Climate information at high spatial and temporal resolution is extremely valuable for understanding future climate changes and variability, especially for sectors like renewable energy. Our model predicts downscaled ESM simulations that enable more accurate local wind-energy forecasts, illustrated in the supplementary material (Figures A.7 and A.8).

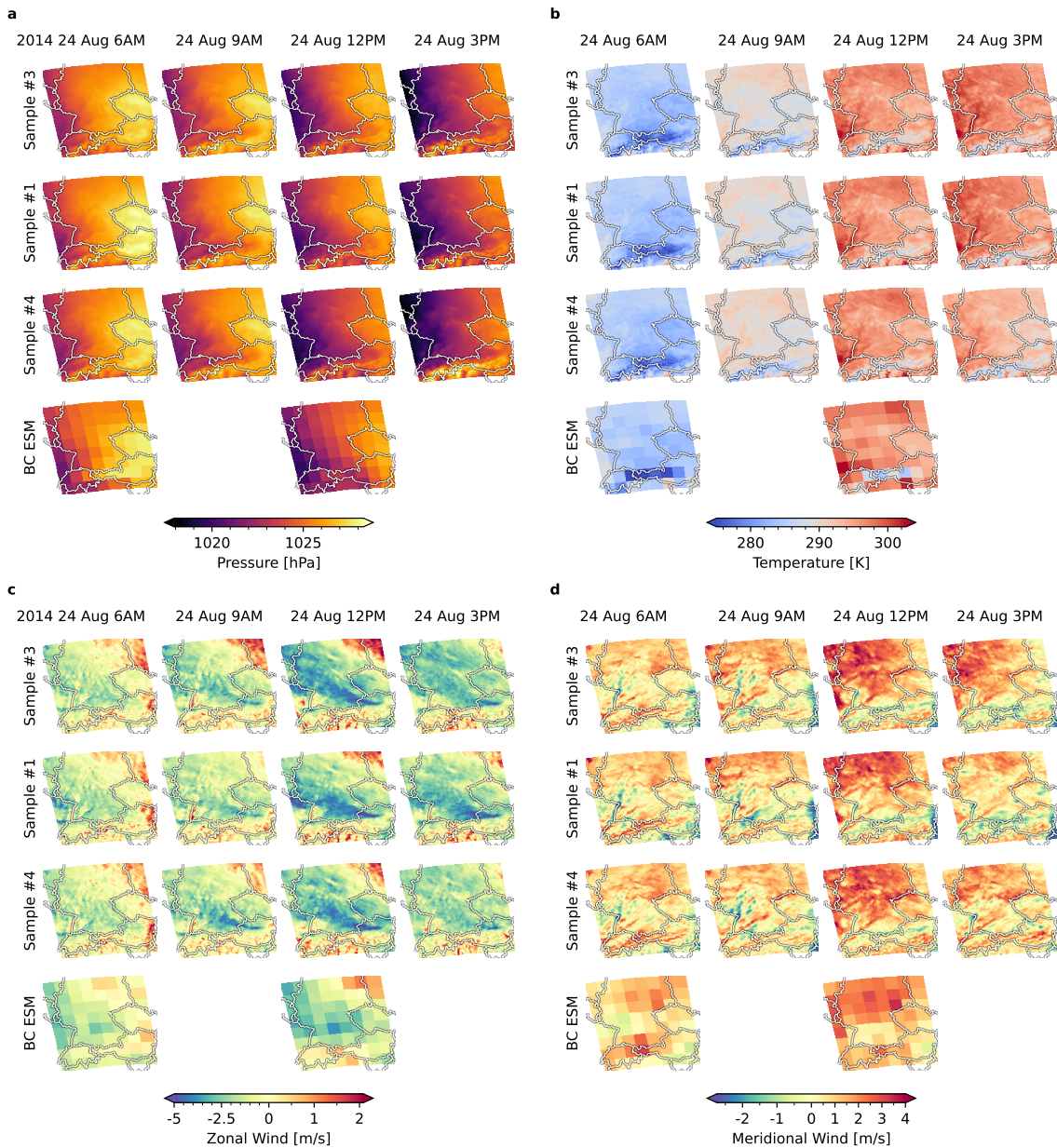


Figure 6: **Local climate information through downscaling.** The plot shows spatiotemporally downscaled predictions for the MPI-HR ensemble that is part of the CMIP6 simulations. Time progresses from left to right in three-hourly steps, starting 2014 August 24 at 06:00 AM and ending the same day at 03:00 PM. The four variables, mean sea-level pressure (**a**), surface temperature (**b**), and zonal (**c**) and meridional (**d**) wind-speed components are downscaled jointly by the model. The top three rows show the progression of three randomly selected samples. The bottom row shows the corresponding conditioning information from the coarse bias-corrected (BC) ESM simulations. Where the observation is blank, the model interpolates in time, without any conditioning information.

Discussion

We introduced a probabilistic approach to joint spatial and temporal downscaling of multiple variables from climate to weather scale. The presented framework allows for using a trained generative model, which acts as a physical prior, in combination with an observation model that is formulated independent of the model training, and which defines the inference task. For our purpose, we leveraged this mechanism to encode a direct relationship between climate simulations and generated weather dynamics, such that the predicted small-scale phenomena preserve the statistics of the climate simulations. Our results provide a methodological advancement into joint spatial and temporal downscaling of multiple variables from ESM simulations to the weather scale.

High spatial and temporal resolution climate information is essential for impact assessment and decision-making on local scales, particularly in sectors sensitive to climate variability [12]. For instance, our approach can generate spatially and temporally consistent, multivariate scenarios that provide insights for critical infrastructure sectors such as agriculture, water resources, and renewable energy [13]. We briefly sketch out an example of the many potential downstream tasks by demonstrating the value of local climate information to estimate wind energy potentials [see for example 10]. We find that, locally, observational wind speed distributions differ substantially from the coarse ESM data, which can result in large differences in predicted wind power generation and accumulated yearly wind energy output. In the supplementary material (Figure A.7), we illustrate that the downscaled predictions preserve the globally-averaged generated wind power, while locally, the estimates move closer to the reanalysis data. Thereby, the model corrects the predicted wind power when under- and over-estimated ESM wind power occurs. Beyond that, estimating small-scale temporal information, which preserves long-term global properties of the guiding ESM simulation, could prove useful for studying different types of extreme events, for example, heat waves [14–17] or flooding events and hazards [18–20].

Current approaches to providing small-scale climate simulations concentrate on downscaling spatial snapshots for single variables [for example 21–25] and thus output de-coupled sequences of temporally independent states. Our approach closes this gap in that the jointly sampled multivariate predictions are each spatially, temporally, and physically coherent weather-scale climate trajectories. Further, existing work focuses on mapping between different reanalysis data sets [26, 27]. Our approach differs because we explicitly developed a model for unpaired samples that maps between different climate scenarios from ensembles from the CMIP6 project to realistic local weather patterns.

The generative model used in this study separates a trained physical prior model from the observations model; the latter specifies the inference task, depending on the application at hand. Thus, unlike approaches that require training the model directly on the conditioning information, the presented framework allows the formulation of explicit—and varying—functional relationships between observations and predictions. We see high future potential in encoding additional, potentially more complex, problem-specific domain knowledge through the observation model in subsequent studies that build upon the present work. For instance, one could encode known functional relationships between the predicted climate variables and external forcing, such as CO₂ concentrations. It is a feature of the modular composition of the framework (Figure 1) that the trained score model can be directly re-used in follow-up research. Trained weights, the model, and the implementations of the methods and experiments are provided at <https://github.com/schmidtjonathan/Climate2Weather>.

Sampling spatiotemporally consistent trajectories requires increased computational cost compared

to alternative approaches. While we have extended the original method by Rozet and Louppe [6] in terms of scalability, enabling it to process substantially longer trajectories, the temporal and spatial extent of the study is still limited by computational demands. This study limits itself to a small region with a diverse range of orography to establish and validate the methodological framework. However, we believe that long-range teleconnections that affect the sub-region under study are, to some extent, reflected in the predictions, given that the training data has been drawn from a Europe-wide reanalysis dataset. This argument is visually supported by embedding high-resolution predictions into a larger spatial context of reanalysis data in the supplementary Figures A.3 to A.6.

The presented framework provides a flexible and powerful foundation for inference tasks in meteorology and climate science by separating between (1) capturing patterns from the learned dynamics and (2) imposing constraints through flexible and cheap conditioning. The model thus provides a step towards making long-term coarse-grained climate projections available for studying the impacts of anthropogenic climate change on local and multiple temporal scales.

Methods

Data

We analyze four closely interrelated atmospheric variables, namely the zonal (`uas`) and meridional (`vas`) components of near-surface wind speeds estimated at 10 meters height, surface air temperature (`tas`), and sea level pressure (`psl`) due to their crucial importance for understanding atmospheric dynamics. They evolve on different spatial and temporal scales, enabling insights into the performance of downscaling methods across different scales.

Reanalysis data For training (2006-2013) and evaluation (2014) of the model, we use data from the Consortium for Small-Scale Modeling Reanalysis 6 (COSMO-REA6) product that is a high-resolution reanalysis product for the European domain developed by the Deutscher Wetterdienst (DWD) [28] with a spatial resolution of approximately 6 km and hourly temporal resolution. It serves as the ground truth observational dataset in the on-model evaluation of the presented methodological framework. The COSMO-REA6 data contains errors for some variables and lacks some observations for the years prior to 2006. In this work, only data from 2006 onwards was used.

Climate model data We apply our downscaling model to historical model runs from two established general circulation models (GCMs) that are part of the sixth phase of the Coupled Model Intercomparison Project (CMIP6) [2], namely the higher-resolution earth system model (ESM) of the Max-Planck Institute (MPI-ESM1.2-HR) [29] and the high-resolution configuration of the third Hadley Centre Global Environment Model in the global coupled configuration 3.1 (HadGEM3-GC3.1-LM) [30]. Both models have an approximately 100 km spatial and 6-hourly temporal resolution.

We restrict our analysis to the spatial subregion including parts of Germany, Switzerland, Austria and Czech Republic (6° E – 16° E, 46° N – 52° N (see supplementary Figure A.1) which results in 128×128 gridpoints per time point for the reanalysis dataset. We use data for the period 2006-2014, the time range in which the reanalysis and the historical GCM runs overlap. The GCM data is spatially re-gridded to a rotated latitude-longitude grid using bilinear interpolation to match the coordinates and grid type of the reanalysis dataset.

Model

The core of the presented methodological framework is a score-based diffusion model (DM) [31, 3, 4, 32, 33], an instance of generative models that involves training a deep neural network on a finite set of data points and can then be used to generate samples from the underlying data distribution. The basic formulation of DMs involves two main components. Firstly, a forward *diffusion process* transports the data distribution to a known, tractable distribution, such as, a standard normal distribution [3, 4]. In this process, structured data points (like RGB images, weather variables, etc.) are successively perturbed until all signals are entirely replaced by noise. The pivotal insight is that a certain class of diffusion processes are known to have a time-reversed counterpart, providing a generative process that successively refines samples from the noise distribution into structured data. The reversal of the diffusion process requires access to the *score function*, which can be understood as a function that, for any given degree of perturbation during the reverse-time diffusion process, separates noise from the signal to remove it. In the following, we will give a brief overview of the general framework and the extensions to it necessary to obtain the results presented in this work.

The considered class of diffusion processes are Gauss–Markov processes that are the solution to linear stochastic differential equations of the form [34]

$$dX(\tau) = FX(\tau)d\tau + LdW(\tau), \quad X(0) \sim \mathcal{N}(X_0, \Sigma_0). \quad (1)$$

The state $X(\tau)$ at $\tau = 0$ is a data point $X_0 \sim \mathcal{D}$ selected from a data set \mathcal{D} . The datum is successively perturbed through the diffusion process and thus loses all structure as $\tau \rightarrow T$. Note that τ is sometimes referred to as "time", which does not mean physical time but rather a continuous degree of perturbation of the initial state. The drift F and dispersion L define functional properties of the forward process, which is driven by Brownian motion $W(\tau)$. At a final time step T (often $T = 1$), the process converges to a Gaussian distribution such that $X(T) \sim \mathcal{N}(0, \Pi)$, where the final-step covariance Π depends on the choice of F and L and is often modeled to be the identity matrix. From a result by Anderson [35] the reverse process of Equation (1) is known and given as

$$dX(\tau) = \left[FX(\tau) - LL^\top \underbrace{\nabla_{X(\tau)} \log p_\tau(X(\tau))}_{\text{score function}} \right] d\tau + Ld\overleftarrow{W}(\tau), \quad X(T) \sim \mathcal{N}(0, \Pi). \quad (2)$$

This process is driven by reverse-time Brownian motion $\overleftarrow{W}(\tau)$ and depends on the gradient of the log-marginal density, called the *score*, of the diffused state $X(\tau)$ at every perturbation-time point τ . We call Equation (2) the *generative process* as it allows sampling unseen data points from the data distribution simply by

1. sampling a vector of independent Gaussian noise $X(T) \sim \mathcal{N}(0, \Pi)$
2. numerically simulating Equation (2) backwards through time, starting from $X(T)$ and ending at a generated sample $X(0)$.

There is much existing and active research regarding the sampling algorithm used in step 2., which, in general, is slower and more complex when comparing diffusion models to other methods from the generative-model class [36–38]. This work uses a standard technique that solves an ordinary differential equation related to the marginal distribution of Equation (2), instead [5, 4, 33].

In practice, the score of $p_\tau(X(\tau))$ is not accessible and has to be estimated. It is common practice to train a time-dependent neural network $s_\theta(X(\tau), \tau)$ on a finite set of samples from the data distribution to approximate the true, intractable score function. Most practical approaches optimize a de-noising score-matching objective [39, 3, 5, 4, 32, 33]. In light of this, simulating Equation (2) is commonly perceived as iteratively de-noising the initial Gaussian random state $X(T)$ and successively refining it to a noise-free data point. For spatial data, a time-conditioned U-Net [40, 3] architecture has proven effective in modelling the score function. The U-Net architecture consists of multiple levels, each containing blocks of convolutional layers and skip connections. Along these levels, the spatial dimensionality of the input data is first successively reduced and then increased again. This encoder-decoder structure results in a bottleneck layer that forces the model to extract a limited set of meaningful features from the input. At each level, skip connections between equal-resolution blocks are introduced to facilitate the learning task by maintaining information throughout the encoding- and decoding process. This work uses a U-Net architecture with a total number of around 72 million parameters, including a self-attention mechanism at the 8×8 -bottleneck layer [3, 41].

The framework used in the presented experiments is centered around the work by Rozet and Louppe [6] that extends the basic DM framework, enabling robust sampling from a posterior distribution and generating arbitrary-length sequences of spatiotemporally coherent state trajectories. The idea behind score-based data assimilation (SDA) is to separate an inference task into two parts:

- I. learning a generative physical model that reproduces spatiotemporal patterns from the desired output space and
- II. conditioning the prior model using a functional constraint (the observation model) to solve a specific task.

In our case, the output space is that of high-resolution, multivariate spatiotemporal weather dynamics, so we train the physical model on reanalysis data. Regarding I., the score model is trained on and learns to generate short temporally and spatially coherent trajectories. Through an intricate convolution-like routine, the windows are assembled into trajectories of arbitrary length. De-noising each time step in the trajectory is computed using a short temporal context window around that time step. This yields output dynamics that are temporally coherent without the need for training the network on long sequences, which would not only significantly increase the computational complexity but also fix the number of time steps as a pre-determined hyperparameter, greatly limiting flexibility. We refer to Rozet and Louppe [6, Algorithm 2] for details and pseudo-code.

For our experiments, we require scaling the original SDA framework to allow for the prediction of very long time horizons with thousands of steps. Unfortunately, sampling a spatiotemporally coherent trajectory in the described manner comes at an increased computational cost and, in particular, significant memory demands since the entire state trajectory must be held in memory. To make the approach scale to predicting 1-hourly weather dynamics for multiple years, we implement the spatiotemporal score function as a massively parallelized convolution operation through time that efficiently manages the available memory—optionally on multiple devices. This extension of the original implementation has proven indispensable for the problem scale. The corresponding Python implementation is provided at <https://github.com/schmidtjonathan/Climate2Weather>.

The generative model described above can generate random sequences of weather-like patterns. One can think of it as a physical prior in that it represents a model for the general spatial and temporal

patterns observed in high-resolution weather dynamics. To tackle the downscaling task specifically, we need the second component (II.) of the SDA method, which allows us to impose the constraints provided by the coarse ESM simulations onto this prior model. This is achieved by conditioning the trained score model. Concretely, while the unconditioned diffusion model generates samples $p(X(0))$, we want to sample from a posterior $p(X(0) | Y)$, instead. To that end, we formulate an observation model $p(Y | X(0))$ that relates coarse input Y to $X(0)$. We consider a Gaussian observation model

$$p(Y | X(0)) = \mathcal{N}(Y; h(X(0)), R), \quad (3)$$

with observation operator $h(X(0))$ that can be a linear or non-linear function [42, 6]. In our case, h selects from the high-resolution state X every six hours and computes a patch-wise averaging in space. Concretely, we thereby encode the assumption that each grid point at each step in the ESM simulation corresponds to the average of a surrounding spatial region of 16×16 grid points that is observed once every six hours. For our experiments, the observation noise R is selected by running a simple random search on a range of plausible values. To accelerate model selection, we chose R based on the model’s performance when recovering small-scale information from a two-day window of coarsened reanalysis data. The resulting observation model is used in all presented experiments. Sampling from $p(X(0) | Y)$ amounts to replacing the score function in Equation (2) by a posterior score function $\nabla_{X(\tau)} \log p_\tau(X(\tau) | Y)$. For details, we refer the reader to [42], who establish the concept of "Diffusion Posterior Sampling" and to its extension by Rozet and Louppe [6]. To make the conditioning work efficiently at the problem scales considered in our experiments, we use an approximation in the conditioning mechanism, which is described and derived in Appendix A.6.

Experimental Setup

Model Evaluation ESM projections are not directly paired to reanalysis data, so we begin by evaluating the generative downscaling model in an on-model setting. We set up an experimental setting that allows us to compare the model output to a ground truth to assess its predictive performance. Firstly, the model is trained on a subset (2006–2013) of the COSMO reanalysis data. A separate subset (2014) serves as a test set. Then, ...

1. ... from the test set, we select two days (starting 07 April 2014 at 04:00 AM) and generate artificial coarse observations that represent ESM projections. The spatial resolution is reduced by a factor of 16 and the temporal resolution by a factor of 6. Specifically,
 - (a) every 6th time step (hour) is selected from the ground truth,
 - (b) a patch-wise spatial averaging operation is applied throughout the spatial region at every time step. We compute the arithmetic mean for each 16×16 spatial patch to yield a single spatial observation.
2. With the observations from 1., the model predicts the underlying 1-hourly, high-resolution weather dynamics lost by coarsening the data. Multiple samples are drawn.
3. The two samples are compared to the reanalysis data from the same time period and evaluated. Variations between the samples imply structured uncertainty.

The predicted results from 3. are analyzed regarding their spatial, temporal, and physical consistency with the reanalysis data, their predictive accuracy, and their uncertainty quantification.

Downscaling CMIP6 As a second step, ESM (CMIP 6) simulations will exchange the artificially coarsened reanalysis data for the final experiment. Instead of artificially spatiotemporally subsampled reanalysis data, we condition the score model on two different ensembles from the CMIP 6 data set: the MPI-HR and the HadGEM3 runs. The experimental setup is adopted exactly from the on-model experiments, aside from the ESM conditioning information and the extended considered time horizon of one full year. Concretely, we downscale the ESM simulations for the considered spatial patch from January 1, 06:00 AM until December 31, 06:00 AM (8 736hours) for the year 2014, increasing the spatial resolution from 8×8 ($\sim 100\text{km}$) to 128×128 ($\sim 6\text{km}$) grid points. For the four high-resolution variables, this corresponds to a total of $4 \times 8\,736 \times (128 \times 128) = 572\,522\,496$ predicted values given conditioning information that is coarser by a factor of $(16 \times 16) \times 6 = 1\,536$. For this specific experiment, we used four NVIDIA A-100 GPUs, each of which generated two predictions in parallel. Generating one 1-year sample of hourly downscaled predictions for the 128×128 -node region takes around two hours on a single NVIDIA A-100 device.

Code availability

The code (in Python) for model training and evaluation, data processing, and for reproducing all presented experiments and figures contained in this manuscript, is available at <https://github.com/schmidtjonathan/Climate2Weather>.

Bibliography

- [1] Peter Bauer, Alan Thorpe, and Gilbert Brunet. The quiet revolution of numerical weather prediction. *Nature*, 525:47–55, September 2015. ISSN 1476-4687.
- [2] Veronika Eyring, Sandrine Bony, Gerald A. Meehl, Catherine A. Senior, Bjorn Stevens, Ronald J. Stouffer, and Karl E. Taylor. Overview of the Coupled Model Intercomparison Project Phase 6 (CMIP6) experimental design and organization. *Geosci. Model Dev.*, 9(5):1937–1958, May 2016. ISSN 1991-959X.
- [3] Jonathan Ho, Ajay Jain, and Pieter Abbeel. Denoising diffusion probabilistic models. In H. Larochelle, M. Ranzato, R. Hadsell, M.F. Balcan, and H. Lin, editors, *Advances in Neural Information Processing Systems*, volume 33, pages 6840–6851. Curran Associates, Inc., 2020.
- [4] Yang Song, Jascha Sohl-Dickstein, Diederik P Kingma, Abhishek Kumar, Stefano Ermon, and Ben Poole. Score-based generative modeling through stochastic differential equations. In *International Conference on Learning Representations*, 2021.
- [5] Jiaming Song, Chenlin Meng, and Stefano Ermon. Denoising diffusion implicit models. In *International Conference on Learning Representations*, 2021.
- [6] François Rozet and Gilles Louppe. Score-based data assimilation. In A. Oh, T. Naumann, A. Globerson, K. Saenko, M. Hardt, and S. Levine, editors, *Advances in Neural Information Processing Systems*, volume 36, pages 40521–40541. Curran Associates, Inc., 2023.
- [7] Douglas Maraun. Bias correction, quantile mapping, and downscaling: Revisiting the inflation issue. *Journal of Climate*, 26(6):2137–2143, 2013.

- [8] Douglas Maraun. Bias correcting climate change simulations—a critical review. *Current Climate Change Reports*, 2(4):211–220, 2016.
- [9] DM Smith, R Eade, AA Scaife, L-P Caron, G Danabasoglu, TM DelSole, T Delworth, FJ Doblas-Reyes, NJ Dunstone, L Hermanson, et al. Robust skill of decadal climate predictions. *Npj Climate and Atmospheric Science*, 2(1):13, 2019.
- [10] Sofia Morelli, Nina Effenberger, Luca Schmidt, and Nicole Ludwig. Climate data selection for multi-decadal wind power forecasts. *arXiv preprint arXiv:2411.11630*, 2024.
- [11] Shipra Jain, Adam A Scaife, Theodore G Shepherd, Clara Deser, Nick Dunstone, Gavin A Schmidt, Kevin E Trenberth, and Thea Turkington. Importance of internal variability for climate model assessment. *npj Climate and Atmospheric Science*, 6(1):68, 2023.
- [12] Thomas Houet, Marine Grémont, Laure Vacquié, Yann Forget, Apolline Marriotti, Anne Puissant, Séverine Bernardie, Yannick Thiery, Rosalie Vandromme, and Gilles Grandjean. Downscaling scenarios of future land use and land cover changes using a participatory approach: an application to mountain risk assessment in the Pyrenees (France). *Reg. Environ. Change*, 17(8):2293–2307, December 2017. ISSN 1436-378X.
- [13] Daniel Adshead, Amelie Paszkowski, Sarah S. Gall, Alison M. Peard, Mohammed Sarfaraz Gani Adnan, Jasper Verschuur, and Jim W. Hall. Climate threats to coastal infrastructure and sustainable development outcomes. *Nat. Clim. Change*, 14:344–352, April 2024. ISSN 1758-6798.
- [14] Zachary Zobel, Jiali Wang, Donald J. Wuebbles, and V. Rao Kotamarthi. High-Resolution Dynamical Downscaling Ensemble Projections of Future Extreme Temperature Distributions for the United States. *Earth’s Future*, 5(12):1234–1251, December 2017. ISSN 2328-4277.
- [15] R. El-Samra, E. Bou-Zeid, H. K. Bangalath, G. Stenchikov, and M. El-Fadel. Seasonal and Regional Patterns of Future Temperature Extremes: High-Resolution Dynamic Downscaling Over a Complex Terrain. *J. Geophys. Res. Atmos.*, 123(13):6669–6689, July 2018. ISSN 2169-897X.
- [16] D. Barriopedro, R. García-Herrera, C. Ordóñez, D. G. Miralles, and S. Salcedo-Sanz. Heat Waves: Physical Understanding and Scientific Challenges. *Rev. Geophys.*, 61(2):e2022RG000780, June 2023. ISSN 8755-1209.
- [17] Valerio Lembo, Simona Bordoni, Emanuele Bevacqua, Daniela I. V. Domeisen, Christian L. E. Franzke, Vera M. Galfi, Chaim I. Garfinkel, Christian M. Grams, Assaf Hochman, Roshan Jha, Kai Kornhuber, Frank Kwasniok, Valerio Lucarini, Gabriele Messori, Duncan Pappert, Iago Perez-Fernandez, Jacopo Riboldi, Emmanuele Russo, Tiffany A. Shaw, Iana Strigunova, Felix Strnad, Pascal Yiou, and Nedjeljka Zagar. Dynamics, Statistics, and Predictability of Rossby Waves, Heat Waves, and Spatially Compounding Extreme Events. *Bull. Am. Meteorol. Soc.*, 105(12):E2283–E2293, December 2024. ISSN 0003-0007.
- [18] Robert J. Trapp, Eric D. Robinson, Michael E. Baldwin, Noah S. Diffenbaugh, and Benjamin R. J. Schwedler. Regional climate of hazardous convective weather through high-resolution dynamical downscaling. *Clim. Dyn.*, 37(3):677–688, August 2011. ISSN 1432-0894.
- [19] Alexander Michalek, James M. Done, and Gabriele Villarini. Future Changes in Regional Tropical Cyclone Wind, Precipitation, and Flooding Using Event-Based Downscaling. *Earth’s Future*, 12(6):e2023EF004279, June 2024. ISSN 2328-4277.

- [20] Joseph W. Lockwood, Ning Lin, Avantika Gori, and Michael Oppenheimer. Increasing Flood Hazard Posed by Tropical Cyclone Rapid Intensification in a Changing Climate. *Geophys. Res. Lett.*, 51(5):e2023GL105624, March 2024. ISSN 0094-8276.
- [21] Luca Schmidt and Nicole Ludwig. Wind power assessment based on super-resolution and downscaling—a comparison of deep learning methods. *arXiv preprint arXiv:2407.08259*, 2024.
- [22] Michael Langguth, Ankit Patnala, Sebastian Lehner, Markus Dabernig, Konrad Mayer, Irene Schicker, GeoSphere Austria, and Paula Harder. A benchmark dataset for meteorological downscaling. In *International Conference on Learning Representations*, 2024.
- [23] Michael Aich, Philipp Hess, Baoxiang Pan, Sebastian Bathiany, Yu Huang, and Niklas Boers. Conditional diffusion models for downscaling & bias correction of Earth system model precipitation. *arXiv*, April 2024.
- [24] Philipp Hess, Michael Aich, Baoxiang Pan, and Niklas Boers. Fast, scale-adaptive, and uncertainty-aware downscaling of earth system model fields with generative foundation models. *arXiv preprint arXiv:2403.02774*, 2024.
- [25] Henry Addison, Elizabeth Kendon, Suman Ravuri, Laurence Aitchison, and Peter AG Watson. Machine learning emulation of precipitation from km-scale regional climate simulations using a diffusion model. *arXiv preprint arXiv:2407.14158*, 2024.
- [26] Paula Harder, Alex Hernandez-Garcia, Venkatesh Ramesh, Qidong Yang, Prasanna Sattigeri, Daniela Szwarcman, Campbell Watson, and David Rolnick. Hard-Constrained Deep Learning for Climate Downscaling. *Journal of Machine Learning Research*, 24(365):1–40, 2023. ISSN 1533-7928.
- [27] Christina Winkler, Paula Harder, and David Rolnick. Climate Variable Downscaling with Conditional Normalizing Flows. *arXiv*, May 2024.
- [28] C. Bollmeyer, J. D. Keller, C. Ohlwein, S. Wahl, S. Crewell, P. Friederichs, A. Hense, J. Keune, S. Kneifel, I. Pscheidt, S. Redl, and S. Steinke. Towards a high-resolution regional reanalysis for the european cordex domain. *Quarterly Journal of the Royal Meteorological Society*, 141(686):1–15, 2015.
- [29] Wolfgang A Müller, Johann H Jungclaus, Thorsten Mauritsen, Johanna Baehr, Matthias Bittner, R Budich, Felix Bunzel, Monika Esch, Rohit Ghosh, Helmut Haak, et al. A higher-resolution version of the max planck institute earth system model (mpi-esm1. 2-hr). *Journal of Advances in Modeling Earth Systems*, 10(7):1383–1413, 2018.
- [30] Martin B Andrews, Jeff K Ridley, Richard A Wood, Timothy Andrews, Edward W Blockley, Ben Booth, Eleanor Burke, Andrea J Dittus, Piotr Florek, Lesley J Gray, et al. Historical simulations with hadgem3-gc3. 1 for cmip6. *Journal of Advances in Modeling Earth Systems*, 12(6):e2019MS001995, 2020.
- [31] Jascha Sohl-Dickstein, Eric Weiss, Niru Maheswaranathan, and Surya Ganguli. Deep unsupervised learning using nonequilibrium thermodynamics. In Francis Bach and David Blei, editors, *Proceedings of the 32nd International Conference on Machine Learning*, volume 37 of *Proceedings of Machine Learning Research*, pages 2256–2265, Lille, France, 07–09 Jul 2015. PMLR.

- [32] Diederik Kingma, Tim Salimans, Ben Poole, and Jonathan Ho. Variational diffusion models. In M. Ranzato, A. Beygelzimer, Y. Dauphin, P.S. Liang, and J. Wortman Vaughan, editors, *Advances in Neural Information Processing Systems*, volume 34, pages 21696–21707. Curran Associates, Inc., 2021.
- [33] Tero Karras, Miika Aittala, Timo Aila, and Samuli Laine. Elucidating the design space of diffusion-based generative models. In S. Koyejo, S. Mohamed, A. Agarwal, D. Belgrave, K. Cho, and A. Oh, editors, *Advances in Neural Information Processing Systems*, volume 35, pages 26565–26577. Curran Associates, Inc., 2022.
- [34] S. Särkkä and A. Solin. *Applied Stochastic Differential Equations*. Cambridge University Press, 2019.
- [35] Brian D.O. Anderson. Reverse-time diffusion equation models. *Stochastic Processes and their Applications*, 12(3):313–326, 1982. ISSN 0304-4149.
- [36] Qinsheng Zhang and Yongxin Chen. Fast sampling of diffusion models with exponential integrator. In *The Eleventh International Conference on Learning Representations*, 2023.
- [37] Yang Song, Prafulla Dhariwal, Mark Chen, and Ilya Sutskever. Consistency models. *arXiv preprint arXiv:2303.01469*, 2023.
- [38] Hongkai Zheng, Weili Nie, Arash Vahdat, Kamyar Aizzadenesheli, and Anima Anandkumar. Fast sampling of diffusion models via operator learning. In Andreas Krause, Emma Brunskill, Kyunghyun Cho, Barbara Engelhardt, Sivan Sabato, and Jonathan Scarlett, editors, *Proceedings of the 40th International Conference on Machine Learning*, volume 202 of *Proceedings of Machine Learning Research*, pages 42390–42402. PMLR, 23–29 Jul 2023.
- [39] Pascal Vincent. A connection between score matching and denoising autoencoders. *Neural Computation*, 23(7):1661–1674, 2011.
- [40] O. Ronneberger, P.Fischer, and T. Brox. U-net: Convolutional networks for biomedical image segmentation. In *Medical Image Computing and Computer-Assisted Intervention (MICCAI)*, volume 9351 of *LNCS*, pages 234–241. Springer, 2015.
- [41] Prafulla Dhariwal and Alexander Quinn Nichol. Diffusion models beat GANs on image synthesis. In A. Beygelzimer, Y. Dauphin, P. Liang, and J. Wortman Vaughan, editors, *Advances in Neural Information Processing Systems*, 2021.
- [42] Hyungjin Chung, Jeongsol Kim, Michael Thompson Mccann, Marc Louis Klasky, and Jong Chul Ye. Diffusion posterior sampling for general noisy inverse problems. In *The Eleventh International Conference on Learning Representations*, 2023.
- [43] Evan Ruzanski and V Chandrasekar. Scale filtering for improved nowcasting performance in a high-resolution x-band radar network. *IEEE transactions on geoscience and remote sensing*, 49(6):2296–2307, 2011.
- [44] Lucy Harris, Andrew T. T. McRae, Matthew Chantry, Peter D. Dueben, and Tim N. Palmer. A generative deep learning approach to stochastic downscaling of precipitation forecasts. *Journal of Advances in Modeling Earth Systems*, 14(10), 2022.
- [45] Philipp Hess, Stefan Lange, Christof Schötz, and Niklas Boers. Deep learning for bias-correcting cmip6-class earth system models. *Earth’s Future*, 11(10):e2023EF004002, 2023.

- [46] S. Pulkkinen, D. Nerini, A. A. Pérez Hortal, C. Velasco-Forero, A. Seed, U. Germann, and L. Foresti. Pysteps: an open-source python library for probabilistic precipitation nowcasting (v1.0). *Geoscientific Model Development*, 12(10):4185–4219, 2019.
- [47] Sabine Haas, Uwe Krien, Birgit Schachler, Stickler Bot, Velibor Zeli, Florian Maurer, Kumar Shivam, Francesco Witte, Sasan Jacob Rasti, Seth, and Stephen Bosch. windpython/windpowerlib: Update release, February 2024. URL <https://doi.org/10.5281/zenodo.10685057>.
- [48] C. Carrillo, A.F. Obando Montaña, J. Cidrás, and E. Díaz-Dorado. Review of power curve modelling for wind turbines. *Renewable and Sustainable Energy Reviews*, 21:572–581, 2013. ISSN 1364-0321.
- [49] Thomas Vandal, Evan Kodra, and Auroop R Ganguly. Intercomparison of machine learning methods for statistical downscaling: the case of daily and extreme precipitation. *Theoretical and Applied Climatology*, 137:557–570, 2019.
- [50] Sebastian Bischoff, Alana Darcher, Michael Deistler, Richard Gao, Franziska Gerken, Manuel Gloeckler, Lisa Haxel, Jaivardhan Kapoor, Janne K Lappalainen, Jakob H Macke, et al. A practical guide to sample-based statistical distances for evaluating generative models in science. *Transactions on Machine Learning Research*, 2024.
- [51] Z. Wang, E.P. Simoncelli, and A.C. Bovik. Multiscale structural similarity for image quality assessment. In *The Thrity-Seventh Asilomar Conference on Signals, Systems & Computers, 2003*, volume 2, pages 1398–1402 Vol.2, 2003.
- [52] W Feller. On the theory of stochastic processes, with particular reference to applications. In *First Berkeley Symposium on Mathematical Statistics and Probability*, pages 403–432, 1949.

A Supplementary Text and Figures

A.1 Spatial region: coarse and fine grid

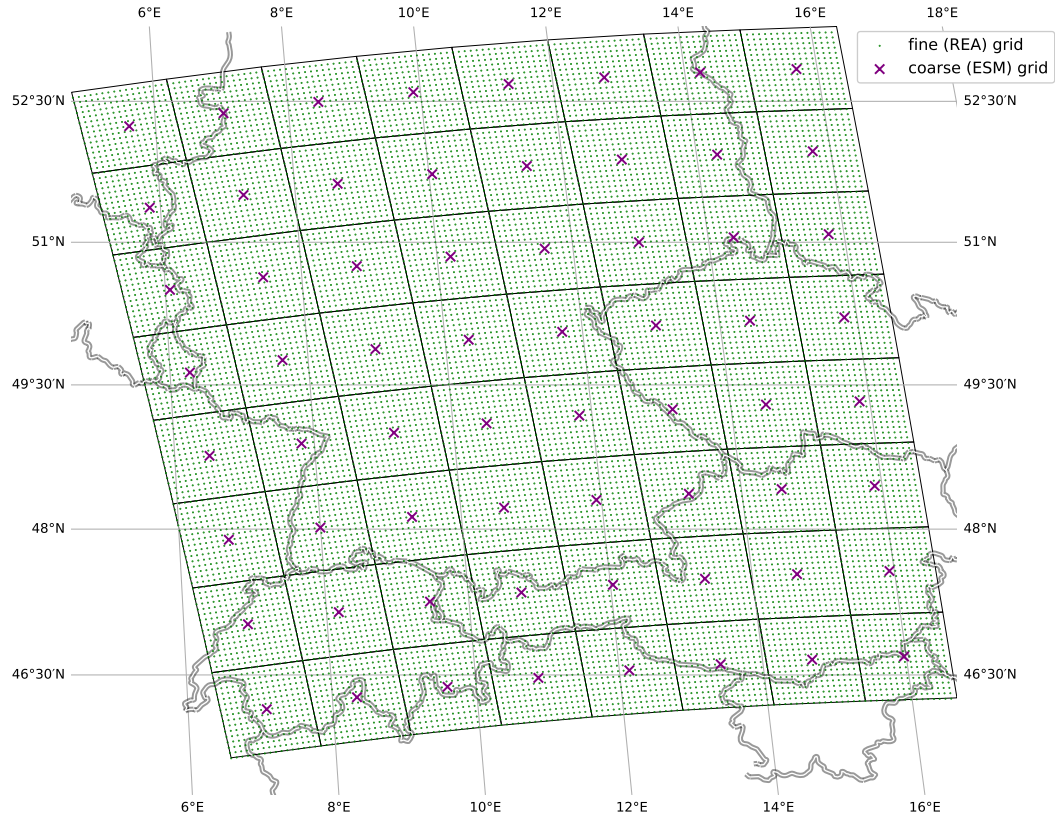
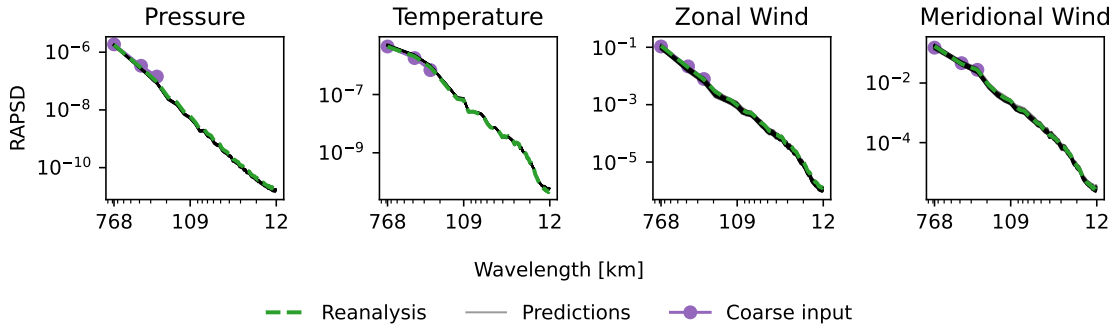


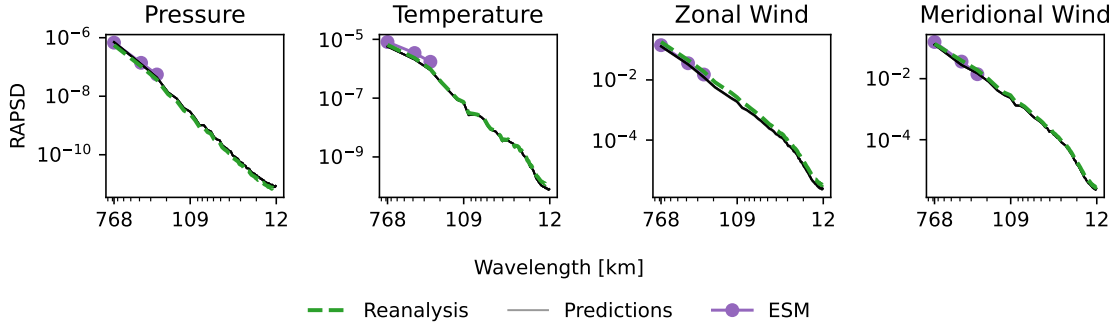
Figure A.1: This plot shows the spatial region considered in this study. The coarse 8×8 -node grid is marked with purple crosses. The fine 128×128 -node grid is marked with green dots. Each coarse-grid node lies in the center of a corresponding 16×16 -patch of high-resolution grid nodes. Both grids span exactly the same area.

A.2 Spatial patterns on multiple scales

To assess the performance of the downscaling model across multiple spatial length scales, we show that the radially-averaged power spectral densities (RAPSD) [43] of the predictions align with the reanalysis data in Figure A.2. The RAPSD is computed by averaging the power spectrum over all directions of the same wavenumber in Fourier space. The quantity is commonly used in the context of weather dynamics, especially when estimating precipitation [44, 45, for example]. We use the open-source `pysteps` package by Pulkkinen et al. [46] to compute the RAPSD. The reported RAPSD values are averages over the considered time period.



(a) RAPSD for reanalysis data, coarse input, and predicted fine-grained reanalysis data.



(b) RAPSD for reanalysis data, CMIP6 simulations, and downscaled CMIP6 simulations.

Figure A.2: This plot shows the RAPSD for reanalysis data, coarse input, and the corresponding downscaled predictions. Subplot (a) mirrors the experimental setup of the on-model experiment that predicts high-resolution reanalysis data during the cyclone "Friederike" in January 2018. Subplot (b) covers the CMIP6-downscaling setup as described in the Methods section.

A.3 Embedding the predicted region in an extended spatial context

We embed the high-resolution predictions during the cyclone "Friederike" (c.f. Figure 4) into a larger spatial context in order to learn about how long-distance interconnections between the studied spatial region and its surroundings are captured by the model. We argue that it is likely that our statistical downscaling model is able to capture the global connectedness of weather dynamics that are contained in the reanalysis data it is trained on. Concretely, Figures A.3 to A.6 visualize the spatiotemporal dynamics of downscaled samples, reanalysis data, and conditioning input. Thereby, the spatial region is extended beyond the one considered in this study. Reanalysis data is used to fill in the regions outside of the predicted patch. Clearly visible or implausible transitions at the edges of the patch would indicate that the model predictions do not align with the surrounding spatial context. We find, however, that there is a smooth transition from outside the predicted area to its interior for the generated high-resolution predictions. The generated local dynamics seamlessly fit into the more surrounding context of reanalysis data.

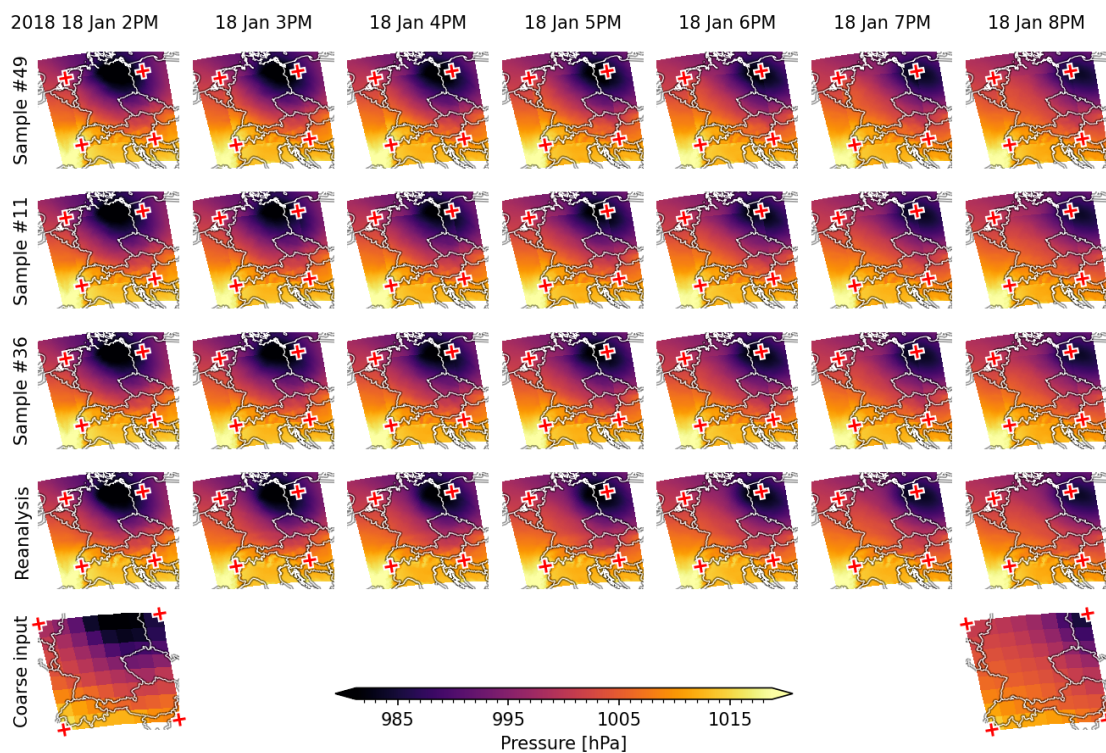


Figure A.3: Predicting mean sea-level pressure during the cyclone "Friederike" (c.f. experiment above). Outside of the prediction range, which lies in the region indicated by red crosses, reanalysis data is filled in to give an impression as to how the predictions fit into more global dynamics.

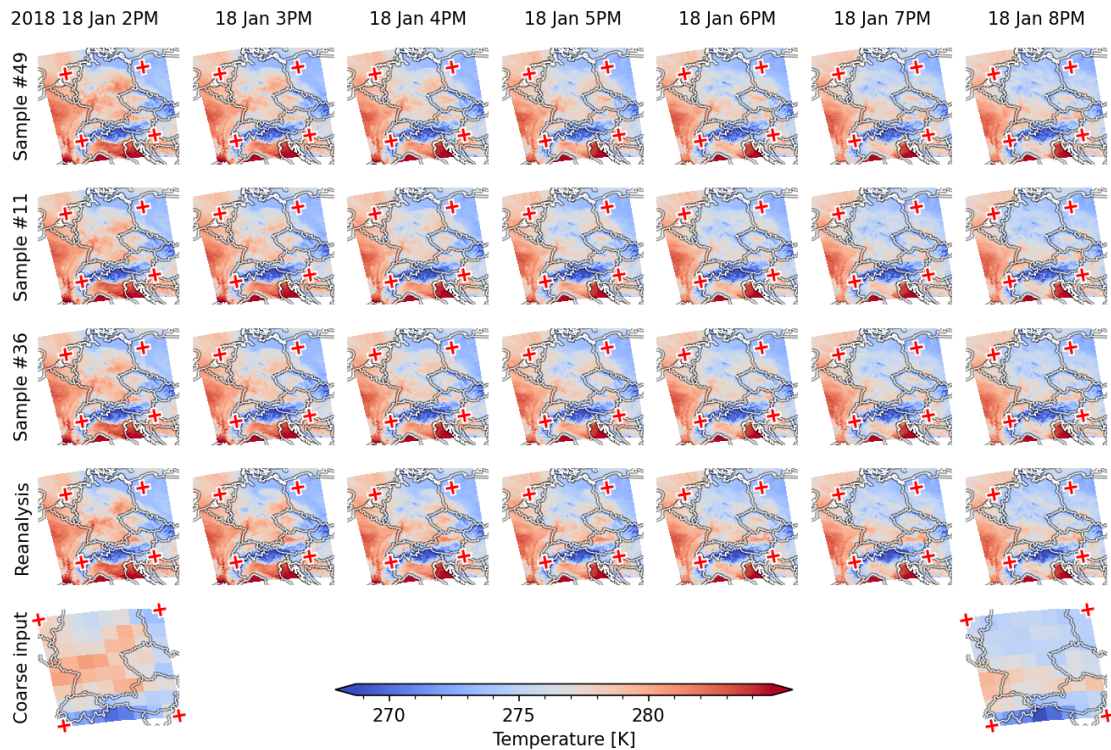


Figure A.4: Predicting surface air temperature during the cyclone "Friederike" (c.f. experiment above). Outside of the prediction range, which lies in the region indicated by red crosses, reanalysis data is filled in to give an impression as to how the predictions fit into more global dynamics.

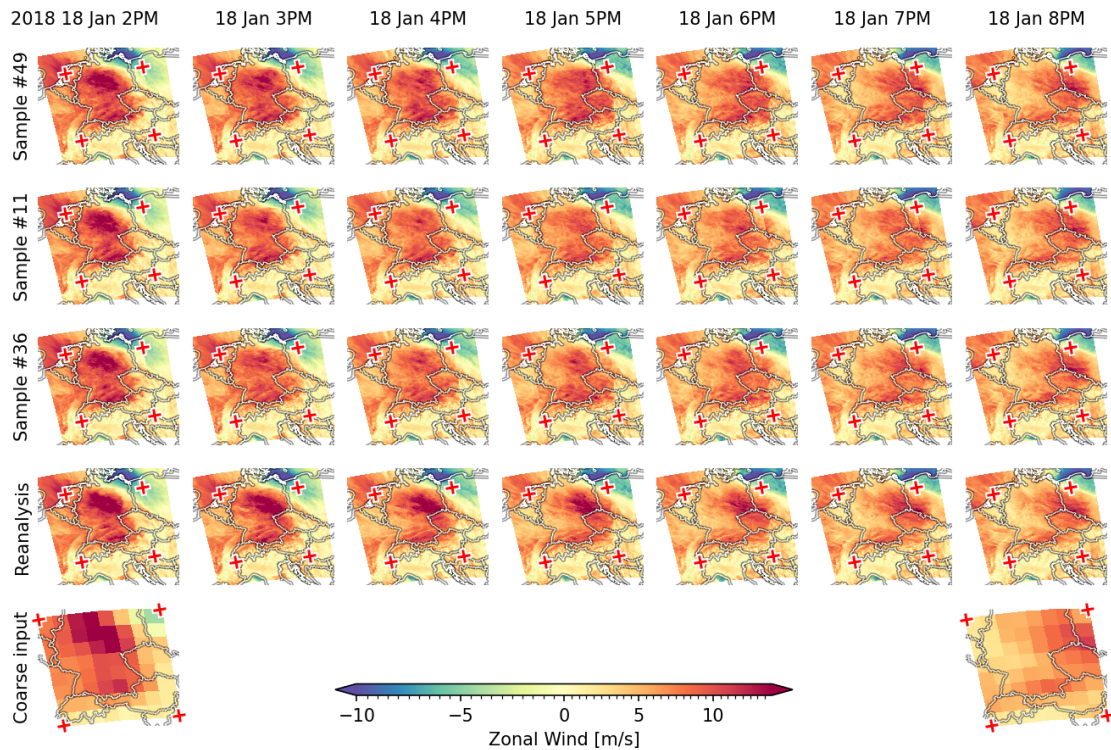


Figure A.5: Predicting meridional wind speed during the cyclone "Friederike" (c.f. experiment above). Outside of the prediction range, which lies in the region indicated by red crosses, reanalysis data is filled in to give an impression as to how the predictions fit into more global dynamics.

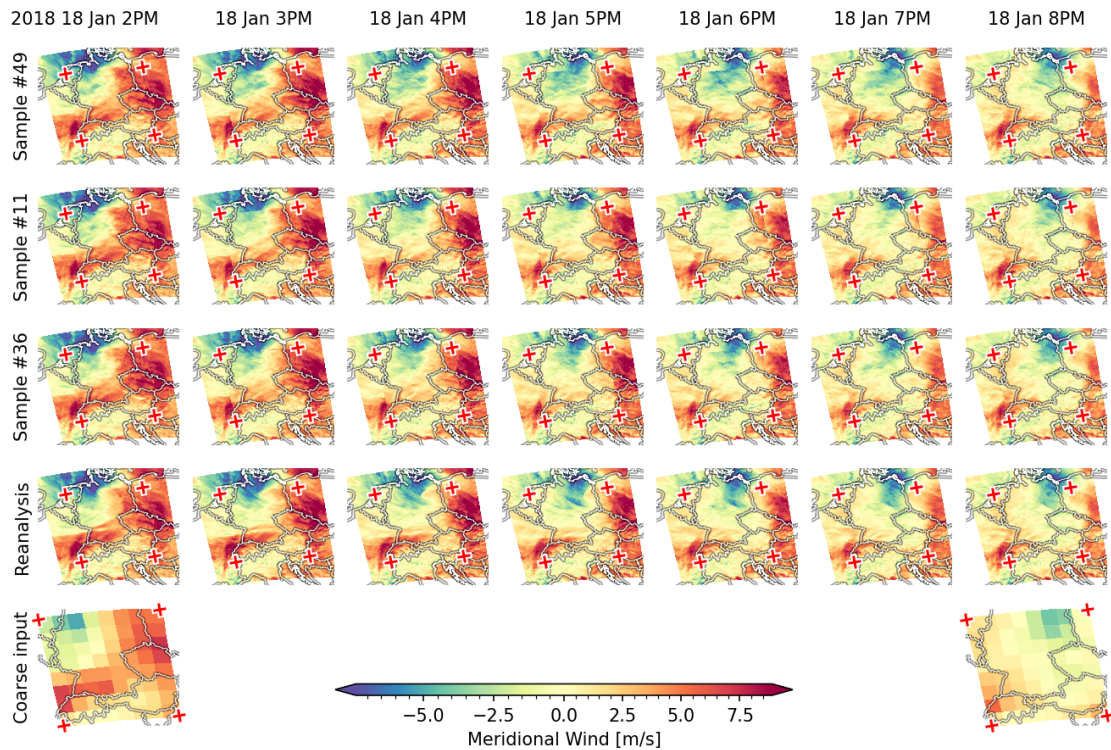


Figure A.6: Predicting zonal wind speed during the cyclone "Friederike" (c.f. experiment above). Outside of the prediction range, which lies in the region indicated by red crosses, reanalysis data is filled in to give an impression as to how the predictions fit into more global dynamics.

A.4 Wind power prediction

A crucial motivation for spatiotemporal downscaling climate simulations to the weather scale are downstream tasks that require future local weather patterns. We provide an exemplary evaluation of the estimated generated wind powers as computed from the CMIP6 simulation, the downscaled predictions, and the reanalysis data. We find that, when computing the spatial average of generated windpowers, the wind-speed and wind-power predictions of the ESM are matched by the downscaled samples in distribution (Figure A.7). Comparing single locations reveals that the ESM locally sometimes over-predicts or under-predicts the wind power generated following the reanalysis data. For both cases, we consistently find that our model corrects the respective over- and under-estimation for multiple randomly-selected locations. We compare estimated densities of the wind-speed values (Figure A.7 a) and use this distribution to derive the amount of wind power generated from the respectively predicted wind speeds (Figure A.7 b). For that, we first compute the wind-power curve for a range of wind-speed values (0m/s to 30m/s), using the open-source package `windpowerlib` [47] and an arbitrary wind-turbine model (turbine type: "E-115/3000", hub-height: 100m). Then, we weigh this power curve with the density of predicted wind speeds to obtain the predicted wind power for each wind speed, taking into account how likely this wind speed value is to occur in the predictions. Finally, we compare the accumulated generated wind power over time. We show the comparison between two pairs of locations in Figure A.8.

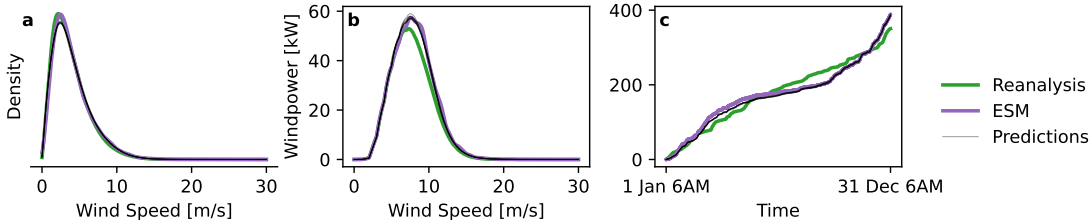
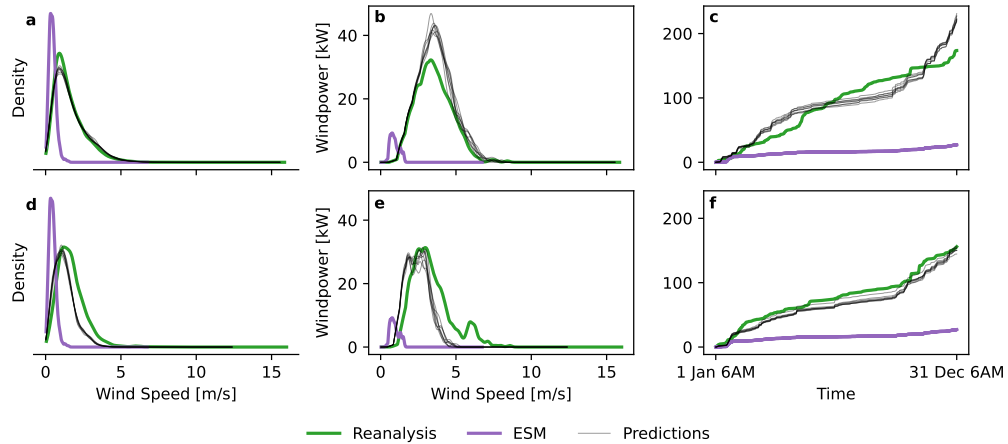
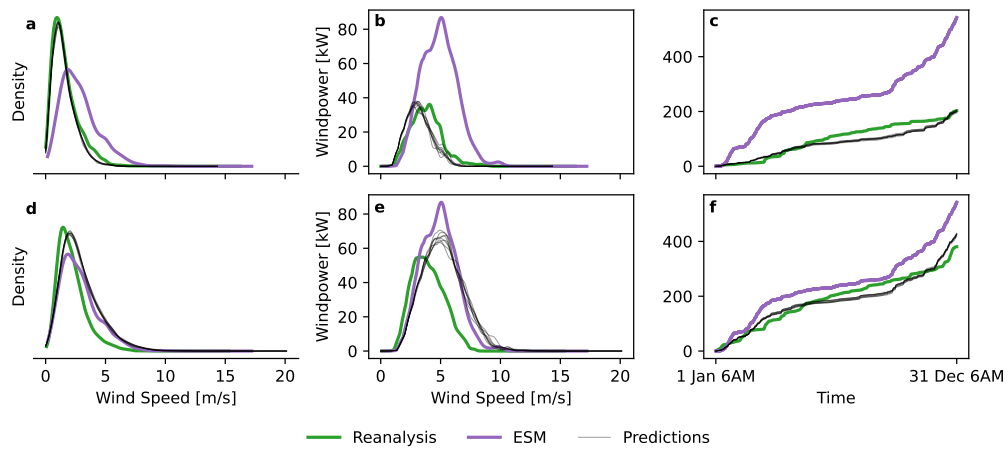


Figure A.7: **Estimated generated wind power over time, averaged over the spatial domain.** This plot analyzes the local wind-speed predictions via the generated wind-power derived from the wind speeds. The full spatial region is considered over the year 2014. Subplot **a** visualizes a kernel-density estimate of the aggregated wind speeds for reanalysis data (green), ESM simulations (purple) and downscaled predictions (black). In **b**, we plot the generated wind power for the entire range of wind speeds from 0m/s to 30m/s, weighted by the density of the estimated wind speeds from **a**. We use a wind-power curve of the form Carrillo et al. [48, Fig. 1]. This estimates the wind power that is generated for the respective wind speeds and accounts for the frequency at which these wind speeds occur. Finally, subplot **c** shows the cumulative sum of the generated wind powers over time. All wind-power values are normalized by the number of time steps on the respective temporal grids to align the wind-power scales. From the black lines aligning closely with the purple line, we conclude that the downscaled predictions preserve the aggregated wind-power generation as simulated by the ESM.



(a) Compare generated windpower at two distinct locations that share a single node on the coarse ESM grid. In this instance, the ESM underpredicts the generated windpower.



(b) Compare generated windpower at two distinct locations that share a single node on the coarse ESM grid. In this instance, the ESM overpredicts the generated windpower.

Figure A.8: Local estimates of wind power over time. This plots investigates two pairs of locations that are each constraint by a single spatial node on the coarse climate grid. The layout of each row of the subplots (a) and (b) mirror [Figure A.7](#); each row corresponds to a single location on the fine-resolution grid, respectively.

A.5 Quantitative evaluation

We first apply quantile-mapping to bias-correct the climate patches. These frames are used as input for the different downscaling algorithms. Our model is compared to the following two baseline approaches.

Baseline 1: Conditioned frame-to-frame diffusion model While our approach leverages a score-based approach, i.e., all states/trajectories are generated simultaneously in a non-autoregressive manner, we compare to a conventional frame-by-frame modeling approach using a denoising diffusion implicit model (DDIM) [5]. We use a time-conditional U-Net backbone, incorporating residual blocks and self-attention layers. The conditioning is then performed by bi-linearly upsampling the bias-corrected climate data to match the high-resolution data and concatenating them along the channel dimension. To predict the middle frame, we condition on a sequence of three frames [21].

Baseline 2: Bias-correction spatial disaggregation The Bias Correction Spatial Disaggregation (BCSD) [49] serves as a baseline due to its simplicity and prominence in the downscaling community. The BCSD method consists of a quantile mapping to correct for biases, followed by bi-linear interpolation to match the spatial resolution of the reanalysis grid. To this end, reanalysis data is first downsampled and remapped to match the coarse resolution of the climate model grid. The bias correction step uses quantile mapping applied to the entire spatial domain. To account for seasonal variations, our implementation uses a moving average (with a window size of 25 days) centered around each calendar day when computing the quantiles. The temporal pooling ensures robust statistics by considering similar days from the seasonal cycle together.

Metrics We use an approximate (sliced) two-dimensional Wasserstein distance [50] as a metric to compare two high-dimensional probability distributions, defined as

$$W(P_{\text{pred}}, P_{\text{ref}}) = \inf_{\gamma \in \Pi(P_{\text{pred}}, P_{\text{ref}})} \mathbb{E}_{(x,y) \sim \gamma} [\|x - y\|_1], \quad (4)$$

where $\Pi(P_{\text{pred}}, P_{\text{ref}})$ is the set of couplings, that is, probability distributions whose marginals are P_{pred} and P_{ref} . This variant makes the traditional Wasserstein distance computationally feasible for high-dimensional probability distributions [50]. In the sliced variant, the high-dimensional data is projected onto a one-dimensional line for which a one-dimensional Wasserstein distance can be efficiently computed. This slicing process is performed repeatedly for multiple different slices and the result is averaged to obtain a reliable metric.

The Mean Energy Log Ratio (MELR) is used to evaluate the preservation of potentially highly varying physical patterns in the downscaled spatial patches. The MELR is a metric that is derived from the radially averaged power spectral density (Appendix A.2) as

$$\text{MELR} = \sum_k \left| \log \left(\frac{E_{\text{pred}}(k)}{E_{\text{ref}}(k)} \right) \right|, \quad (5)$$

where the energy of the predicted field $E_{\text{pred}}(k)$ is compared to that of the reference field $E_{\text{ref}}(k)$.

We use the structural similarity index measure (SSIM) [51], which takes into account perceptual properties of local structures when quantifying the similarity between two spatial data points. The

SSIM is defined by sliding a window $W_k(x, y)$ of size $k \times k$ along the spatial data point that computes for two $k \times k$ -patches x and y

$$W_k(x, y) = \frac{(2\mu_x\mu_y + c_1)(2\sigma_{x,y} + c_2)}{(\mu_x^2 + \mu_y^2 + c_1)(\sigma_x^2 + \sigma_y^2 + c_2)}, \quad (6)$$

where μ_x, σ_x and μ_y, σ_y are the respective average and standard-deviations of the values in the respective patches x and y . Analogously, σ_{xy} is the covariance between the patches. Finally, c_1 and c_2 are constants to make the computation more robust. The SSIM takes on values between 0 and 1, whereby higher values indicate more structural similarities throughout the compared data points. An SSIM of 1 can only be attained when both data points are identical. In [Table A.1](#) we report the SSIM using a window size of $k = 15$.

Table A.1: **Quantitative evaluation of downscaling methods.** We compare the performance of our model, based on score-based data assimilation (SDA), to a conditional denoising diffusion implicit model (DDIM) and to bias-correction spatial disaggregation (BCSD). We report the sliced Wasserstein-1 distance (Sliced W1) over time, temporally averaged energy log ratio (MELR) and structural similarity index (SSIM) for the four variables mean sea-level pressure (**ps1**), surface (2m) air temperature (**tas**), surface (10m) zonal **uas** and meridional (**vas**) wind speeds. The values are reported as mean \pm standard deviation over the generated predictions. Note that, since the baseline methods are not capable of temporal downscaling, the quantitative evaluation is performed on the 6-hourly observation grid. Even though the method proposed in this work is under the additional constraint of generating temporally consistent 1-hourly trajectories, it beats both baselines in most cases. Between all approaches, the best performance per metric and variable is highlighted in **bold**.

Metric \ Method	var	SDA (ours)	BCSD	DDIM
Sliced W1 ↓	ps1	0.3028 \pm 0.0012	0.2900 \pm 0	0.3526 \pm 0.0536
	tas	0.3526 \pm 0.0005	0.3999 \pm 0	0.2894 \pm 0.0999
	uas	0.1998 \pm 0.0015	0.2523 \pm 0	0.4055 \pm 0.0586
	vas	0.2348 \pm 0.0033	0.2702 \pm 0	0.3553 \pm 0.0371
MELR ↓	ps1	1.0256 \pm 0.0031	1.1625 \pm 0	1.0874 \pm 0.1022
	tas	0.3470 \pm 0.0018	1.1312 \pm 0	0.3932 \pm 0.0187
	uas	1.4622 \pm 0.0025	2.4141 \pm 0	1.5598 \pm 0.0770
	vas	1.4555 \pm 0.0096	2.4042 \pm 0	1.3317 \pm 0.0664
SSIM ↑	ps1	0.8925 \pm 0.0002	0.9027 \pm 0	0.8691 \pm 0.0074
	tas	0.8524 \pm 0.0002	0.7066 \pm 0	0.8382 \pm 0.0094
	uas	0.1351 \pm 0.0008	0.0844 \pm 0	0.1182 \pm 0.0061
	vas	0.1322 \pm 0.0009	0.0973 \pm 0	0.1185 \pm 0.0068

A.6 Approximating the gradient of the observation model

Using Bayes' rule, we obtain the posterior score function

$$\nabla_{X(\tau)} [\log p_\tau(X(\tau) | y)] = \nabla_{X(\tau)} [\log p_\tau(X(\tau)) + \log p(Y | X(\tau))] \quad (7)$$

$$= \underbrace{\nabla_{X(\tau)} [\log p_\tau(X(\tau))]}_{\approx s_\theta(X(\tau), \tau)} + \nabla_{X(\tau)} [\log p(Y | X(\tau))]. \quad (8)$$

This illustrates that the conditioning mechanism, which involves only a simple addition of the gradient of the log-observation model, is independent of the trained score model. However, as detailed by Chung et al. [42], the posterior score requires relating the measurement Y to the diffused state $X(\tau)$. Chung et al. [42] propose to approximate

$$p(Y | X(\tau)) = \int p(Y | X(0), X(\tau)) p(X(0) | X(\tau)) dX(0) \quad (9)$$

$$= \int p(Y | X(0)) p(X(0) | X(\tau)) dX(0) \quad (10)$$

$$= \mathbb{E}_{X(0) \sim p(X(0) | X(\tau))} [p(Y | X(0))] \quad (11)$$

$$\approx p(Y | \hat{X}(0) := \mathbb{E}_{X(0) \sim p(X(0) | X(\tau))} [X(0)]). \quad (12)$$

Intuitively, the last step pulls the expectation into the conditioning, which is not equivalent in general, and thereby approximates $p(Y | X(\tau)) \approx p(Y | \hat{X}(0))$. The quantity $\hat{X}(0)$ is a posterior-mean estimate for the noise-free data point underlying the diffused state $X(\tau)$ at the current diffusion-time τ in the generative process. In the following, we detail how $\hat{X}(0)$ is computed.

Linear stochastic differential equations, like the diffusion process defined in Equation (1), can be equivalently formulated in terms of a discrete, linear Gaussian transition model

$$p(X(\tau + \Delta\tau) | X(\tau)) = \mathcal{N}(X(\tau + \Delta\tau); A(\Delta\tau)X(\tau), \Sigma(\Delta\tau)), \quad (13)$$

for some time increment $\Delta\tau$. We refer to, e.g., Särkkä and Solin [34, Section 6.1] for more details on how to derive the *transition* and *process-noise covariance* functions A and Σ from the drift F and dispersion L of the diffusion process (Equation (1)). The forward diffusion process can be simulated over extended time ranges in a single step via sampling from the Gaussian transition density

$$X(\Delta\tau) | X(0) = A(\Delta\tau)X(0) + \Sigma^{\frac{1}{2}}(\Delta\tau)\epsilon, \quad \epsilon \sim \mathcal{N}(0, 1), \quad (14)$$

which is an equivalent formulation of Equation (13) for the case $\tau = 0$, i.e., starting from the noise-free data point [3–5]. The same is not possible in the reverse direction, which would make the generation process trivial. Unfortunately, the backwards transition model associated with Equation (2) is Gaussian only for infinitesimally small time decrements $\Delta\tau \rightarrow 0$ [52, 31], which leads to sampling quality increasing with the number of steps used for simulating the generative process. However, it is possible to estimate the posterior mean $\hat{X}(0)$ based on the current score estimate

$s_\theta(X(\tau), \tau)$. By re-arranging Equation (14) we note that

$$X(0) = A^{-1}(\tau) \left(X(\tau) - \Sigma^{\frac{1}{2}}(\tau)\epsilon \right) \quad (15)$$

$$= A^{-1}(\tau) \left(X(\tau) + \nabla_{X(\tau)} [p_\tau(X(\tau))] \Sigma(\tau) \right) \quad (16)$$

$$\approx A^{-1}(\tau) \left(X(\tau) + s_\theta(X(\tau), \tau) \Sigma(\tau) \right) \quad (17)$$

$$= \hat{X}(0). \quad (18)$$

The first equality uses the direct correspondence between ϵ and the de-noising score function of Equation (13) [3, 32]. Since the true score, like ϵ , is not known while generating a new data point, it is in the next step approximated with our parametric score model s_θ . A more detailed derivation can be found for the scalar case ($A, \Sigma \in \mathbb{R}$) in Chung et al. [42].

With that, we established the necessary background regarding the conditional model, in order to describe the approximation to the conditioning mechanism that is used in this work. Plugging into Equations (7) and (8) the approximation from Equations (9) to (12) reveals that we have to compute the gradient

$$\nabla_{X(\tau)} \left[\log p(Y | \hat{X}(0)) \right]. \quad (19)$$

For our purposes, we assume a Gaussian observation model (Equation (3)), which simplifies this gradient to

$$\nabla_{X(\tau)} \left[\log p(Y | \hat{X}(0)) \right] = \nabla_{X(\tau)} \left[\log \mathcal{N} \left(Y; h(\hat{X}(0)), \mathbf{R} \right) \right] \quad (20)$$

$$= \nabla_{X(\tau)} \left[\|Y - h(\hat{X}(0))\|_{\mathbf{R}} \right], \quad (21)$$

where $\|\cdot\|_{\mathbf{R}}$ is a Mahalanobis norm in the multivariate case and a Euclidean norm in the scalar case. Let us denote the residual between conditioning information and the observed predicted signal as $r(Y, \hat{X}(0)) := Y - h(\hat{X}(0))$. Then, using the chain rule of differentiation, we obtain

$$\nabla_{X(\tau)} \left[\|r(Y, \hat{X}(0))\|_{\mathbf{R}} \right] = \nabla_{r(Y, \hat{X}(0))} \left[\|r(Y, \hat{X}(0))\|_{\mathbf{R}} \right] \cdot \nabla_{\hat{X}(0)} \left[h(\hat{X}(0)) \right] \cdot \nabla_{X(\tau)} \left[\hat{X}(0) \right]. \quad (22)$$

We plug the equality from Equations (17) and (18) into the third component of the gradient to obtain

$$\nabla_{X(\tau)} \left[\hat{X}(0) \right] = \nabla_{X(\tau)} \left[A^{-1}(\tau) \left(X(\tau) + s_\theta(X(\tau), \tau) \Sigma(\tau) \right) \right] \quad (23)$$

$$= A^{-1} \left(1 + \nabla_{X(\tau)} \left[s_\theta(X(\tau), \tau) \Sigma(\tau) \right] \right) \quad (24)$$

$$\approx A^{-1}. \quad (25)$$

The final step approximation avoids the computational demanding differentiation of the score function with respect to the perturbed state, which cuts away the majority of the computational cost in the conditioning. Altogether, the approximate conditioning term (c.f. Equation (8)), used throughout this work, is

$$\begin{aligned} \nabla_{X(\tau)} \left[\log p(Y | X(\tau)) \right] &\approx \nabla_{X(\tau)} \left[\log p(Y | \hat{X}(0)) \right] \\ &\approx \nabla_{r(Y, \hat{X}(0))} \left[\|r(Y, \hat{X}(0))\|_{\mathbf{R}} \right] \cdot \nabla_{\hat{X}(0)} \left[h(\hat{X}(0)) \right] \cdot A^{-1}, \end{aligned} \quad (26)$$

which is very cheap to compute in each de-noising step.